Computation of relativistic and many-body effects in atomic systems using quantum annealing

Vikrant Kumar,[1,*] Nishanth Baskaran,[1] V. S. Prasannaa,[1] K. Sugisaki,[1,2,3] D. Mukherjee,[1] K. G. Dyall,[4] and B. P. Das[1,5]

[1]*Centre for Quantum Engineering, Research and Education, TCG CREST, Salt Lake, Kolkata 700091, India*
[2]*Graduate School of Science and Technology, Keio University, 7-1 Shinkawasaki, Saiwai-ku, Kawasaki, Kanagawa 212-0032, Japan*
[3]*Quantum Computing Center, Keio University, 3-14-1 Hiyoshi, Kohoku-ku, Yokohama, Kanagawa 223-8522, Japan*
[4]*Dirac Solutions, 10527 NW Lost Park Drive, Portland, Oregon 97229, USA*
[5]*Department of Physics, Tokyo Institute of Technology, 2-12-1 Ookayama, Meguro-ku, Tokyo 152-8550, Japan*

(Received 1 March 2023; revised 23 August 2023; accepted 6 March 2024; published 8 April 2024)

We report results for the computation of relativistic effects in quantum many-body systems using quantum annealers. An average accuracy of 98.9% in the fine-structure splitting of boron-like ions with respect to experiments is achieved using the Quantum Annealer Eigensolver (QAE) algorithm on the D-Wave Advantage 5000-qubit hardware, which is substantially higher than that attained on a gate-based quantum device to date. We obtain these results in the framework of the many-electron Dirac theory. We implement QAE using a hybrid quantum annealing method that includes an alternative qubit encoding scheme and decomposing the problem into smaller ones based on perturbation theory.

DOI: 10.1103/PhysRevA.109.042808

I. INTRODUCTION

Quantum annealing (QA) is a metaheuristic for solving optimization problems using quantum effects [1]. It was formulated in its current form by Kadowaki and Nishimori [2] and is steadily gaining in importance. It is related to adiabatic quantum computing, which is considered to be the second paradigm of quantum computing [3–7]. QA can be applied to a wide range of problems [8–14], including the electronic structure of atoms and molecules [15–19]. The recently proposed Quantum Annealer Eigensolver (QAE) algorithm is a promising direction for computing molecular vibrational spectra [17], ground, and excited state energies [18,19]. QAE solves an eigenvalue problem by minimizing a suitable objective function by using the Rayleigh-Ritz variational principle, and has potential applications in many areas of science and engineering and beyond [20–24].

Relativistic effects play a crucial role in various physical and chemical phenomena [25,26]. Their accurate evaluation in quantum many-body calculations is a major challenge, and has important implications in many atomic and molecular problems concerning new physics beyond the standard model of elementary particles [27–32].

Accuracy and speed are two important attributes of any computer including both types of quantum computers: gate-based and quantum annealers. Quantum advantage has not yet been achieved for quantum annealing. In the present work, we attempt to shed light on the accuracy that can be achieved for a relativistic atomic many-body problem using the D-Wave quantum annealer. To this end, we apply the QAE algorithm to determine the fine-structure splitting (FSS) by taking the difference between the minimum energies of two sets of atomic states with the same orbital angular momenta (L, S) but different total angular momentum J. In boron and its isoelectronic systems, the ^2P ground state splits into two odd parity states, one with $J = 1/2$ and the other with $J = 3/2$. In this work, we estimate the lowest-energy state of each set using QAE (simulation and hardware), and the corresponding difference allows us to evaluate the FSS in boron-like ions, which we compare with the measured values of the chosen systems.

FSS is relativistic in origin and is influenced by electron correlation effects [33,34], which are challenging to capture accurately because of the lack of all-to-all connectivity between the qubits of current quantum annealers. Recently, hybrid workflows with quantum annealing and classical components such as QBSOLV [35] have partially alleviated this drawback through decomposition methods, which entail dividing the problem into smaller parts. We adapt the QAE algorithm with certain key workflow improvements to compute the FSS as depicted in Fig. 1. Given that the FSS arises entirely due to relativity, we choose moderately heavy boron-like ions in this work, for which the interplay of relativistic and correlation effects is crucial. Experimental data are available for the specific ions that we have chosen for our computations [36–39].

II. QAE WORKFLOW

A typical QAE calculation can be broken down into three sequential steps: Hamiltonian generation, encoding the functional, and quantum annealing (which subsumes embedding). We generate our Hamiltonian via a differential equation-based approach to solving the multi-configuration Dirac-Fock (MCDF) equations. We note that this route provides the advantage of having a fewer number of single-particle orbitals,

*vikrantkumar.895@gmail.com

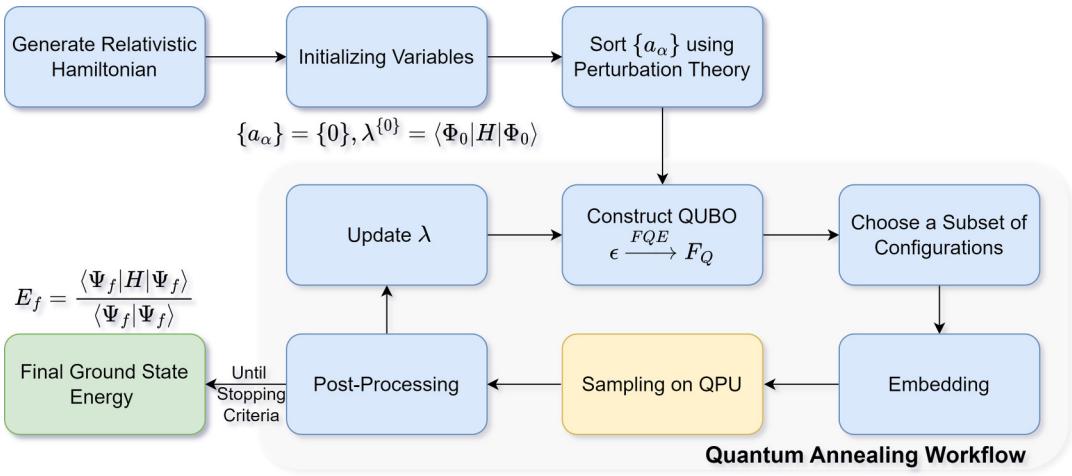

FIG. 1. Illustration of our QAE workflow. The Lagrange multiplier $\lambda^{\{0\}}$ is initialized to the CSF energy associated with the most dominant configuration, $\langle\Phi_0|H|\Phi_0\rangle$. $\{a_\alpha\}$ denotes the list of expansion coefficients from the relativistic CI expansion of the wave function. E_f and $|\Psi_f\rangle$ refer to the final ground-state energy and its corresponding wave function obtained using the presented workflow, respectively. Floating qubit encoding is abbreviated as FQE in the figure.

and hence a smaller configuration interaction (CI) Hamiltonian and fewer coefficients (and therefore cheaper encoding) relative to the matrix formulation approach. For encoding, we employ a floating point encoding scheme. For the quantum annealing step, we introduce a perturbation-theory-based priority sorting as well an alternative approach to updating a parameter, λ. In this section, we introduce our workflow that involves the above-mentioned routines, outlined in Fig. 1.

A. Atomic theory: Hamiltonian generation

The dominant relativistic effects in atomic systems are contained in the Dirac-Coulomb Hamiltonian [40], given as

$$H_{\rm DC} = \sum_i (c\alpha_i p_i + \beta_i c^2 + V_N(r_i)) + \sum_{j>i} \frac{1}{r_{ij}}. \tag{1}$$

The lowest-order relativistic correction to the Coulomb interaction is known as the Breit interaction [41] and whose Hamiltonian is

$$H_B = -\sum_{j>i} \left(\frac{\alpha_i \alpha_j}{2r_{ij}} + \frac{(\alpha_i r_{ij})(\alpha_i r_{ij})}{2r_{ij}^3} \right), \tag{2}$$

where both $H_{\rm DC}$ and H_B are given in atomic units, $V_N(r_i)$ is the potential due to the nucleus, α and β are the Dirac matrices, and c is the velocity of light. r_{ij} is the interelectronic separation. The Dirac-Coulomb-Breit (DCB) Hamiltonian is the sum of the above two Hamiltonians.

The first step in the QAE algorithm is the determination of the matrix elements of the DCB Hamiltonian on a traditional computer. For this purpose, we employ a well-established relativistic atomic structure code [42]. The matrix elements are computed using suitable configuration state functions (CSFs) corresponding to a specific angular momentum (in our case, either $J = 1/2$ or $3/2$) and parity (odd, in this work) as basis functions. These CSFs are built by considering the complete active space (CAS) consisting of single-particle ($1s$, $2s$, $2p_{1/2}$, and $2p_{3/2}$) orbitals. The orbitals are evaluated using a state-averaged calculation within the MCDF method [33], where we used a *common* set of optimized orbitals for the $J = 1/2$ and $J = 3/2$ cases. We extract two submatrices from the CAS Hamiltonian matrix, one built from odd-parity CSFs with $J = 1/2$, while the other is from $J = 3/2$ CSFs, thereby obtaining matrices of size (9×9) and (16×16), for the $^2P_{1/2}$ and the $^2P_{3/2}$ states, respectively. These matrices serve as inputs to the QAE algorithm.

B. Floating point encoding scheme

We begin with the energy functional (ϵ) of interest to us, which is given by

$$\epsilon = \langle\Psi|H_{\rm DCB}|\Psi\rangle - \lambda\langle\Psi|\Psi\rangle, \tag{3}$$

where λ refers to the Lagrange multiplier that guarantees the normalization of the wave function. The wave function can be expressed as a linear combination of CSFs, $|\Psi\rangle = \sum_{\alpha=0}^{\mathcal{B}-1} a_\alpha |\Phi_\alpha\rangle$ (the CSF-based CI approach, which we shall refer to as relCI to indicate that we work in a relativistic framework), where the a_α's denote the expansion coefficients corresponding to the CSFs. Upon minimizing the energy functional with respect to the expansion coefficients, we can obtain the ground-state energy.

Substituting $|\Psi\rangle$ in Eq. (3), we obtain

$$\epsilon = \sum_{\alpha,\beta}^{\mathcal{B}-1} a_\alpha a_\beta H_{\alpha\beta} - \lambda \sum_{\alpha}^{\mathcal{B}-1} a_\alpha^2, \tag{4}$$

where $H_{\alpha\beta} = \langle\Phi_\alpha|H|\Phi_\beta\rangle$. To convert the expression to its quadratic unconstrained binary optimization (QUBO) form for making it compliant with the D-Wave hardware, we represent a_α in the ith Repeat (which will be defined later in this subsection), denoted by $a_\alpha^{\{i\}}$, in binary using K bits through our qubit encoding scheme given by

$$a_\alpha^{\{i\}} = \mu_\alpha + \sigma \sum_{k=0}^{K-1} f_k 2^{-k} q_k^\alpha, \tag{5}$$

where $f_k = -1$ if $k = 0$ and 1 otherwise, and q_i are binary variables. μ_α and σ are updated in each iteration

$$\mu_\alpha = a_\alpha^{\{i-1\}}, \text{ and}$$
$$\sigma = 2^{(-i+1)/2}, \quad \forall\alpha.$$

The initial guess for a_α is set to zero. The second term in Eq. (5) is used as a correction to the previous estimate of a_α (stored as μ_α, which is shifted appropriately with σ to ensure that a_α is within $[-1, 1]$). This is because σ decreases by a factor of $\frac{1}{\sqrt{2}}$ with each iteration, allowing for increasingly smaller values of a_α to be searched for the minimum. The qubit encoding scheme adopted in the present work requires fewer qubits than previous works [17], but the optimization part is performed in an iterative manner till a precision of 10^{-5} is achieved. Fixed point encoding (as used in previous QAE approaches [17]) limits the precision of each a_α by the number of qubits used to represent them, and increasing the number of qubits beyond 10 does not improve results further due to the errors associated with chaining. Hence, capturing coefficients below 10^{-3} becomes difficult with fixed point encoding.

The mapping scheme discussed above increases the Hamiltonian size from $(\mathcal{B} \times \mathcal{B})$ to $(\mathcal{B}K \times \mathcal{B}K)$. The explicit QUBO form after the above conversion is given as

$$F_Q = \sum_{\alpha,\beta=0}^{\mathcal{B}-1} \left(\sum_{n,m=0}^{K-1} q_n^\alpha A q_m^\beta + \sum_{n=0}^{K-1} B q_n^\alpha + C \right), \tag{6}$$

where

$$A = (\sigma^2 f_n f_m 2^{-(n+m)}) H'_{\alpha\beta},$$
$$B = (2\mu_\beta \sigma f_n 2^{-n}) H'_{\alpha\beta},$$
$$C = \mu_\alpha \mu_\beta H'_{\alpha\beta}, \text{ and}$$
$$H'_{\alpha\beta} = (H_{\alpha\beta} - \lambda\delta_{\alpha\beta}).$$

In the above equation, δ_{nm} is 1 if $n = m$ and 0 otherwise.

In our workflow, after Hamiltonian generation, all the coefficients $\{a_\alpha\}$ are set to zero and λ is set to the CSF energy associated with the most dominant configuration, $\langle\Phi_0|H|\Phi_0\rangle$.

In view of the limited connectivity on D-Wave Advantage hardware, the minimization of F_Q is performed through a series of subspace optimizations (each of which in combination with an appropriately chosen value for λ constitutes a "Repeat"), where each subspace corresponds to a subset of coefficients to be optimized, and whose energy landscape is determined by a particular λ. To enable selecting the subset of coefficients in this so-called sub-QUBO based approach, we first determine the CI coefficients approximately using the independent electron pair approximation as $C_\alpha \sim \frac{H_{\alpha 0}}{(H_{00} - H_{\alpha\alpha})}$. We then sort these lists of coefficients in descending order (priority sorting). The indices corresponding to a subset of dominant coefficients are picked for the first Repeat.

C. Quantum annealing

We now elaborate on the "Quantum Annealing Workflow" module from Fig. 1.

As seen in the earlier subsection, we carefully select, say, the first Γ number of dominant coefficients from the sorted list, $\{a_\alpha\}_p \in \{a_\alpha\}$, such that the problem decomposes into as few subproblems as possible, while also ensuring that we do not incur too many Repeats. The corresponding subproblem of the QUBO F_Q is solved by the annealing step, where we set the number of shots (samples) to 1000. Each shot provides a reduced set $\{q\}_r$. From that set, we calculate the reduced set $\{a_\alpha\}_r$, and we merge it with the other coefficients that were not in $\{a_\alpha\}_p$, and by using it we obtain the minimum energy. For each of the subsequent Repeats, λ as well as the choice of coefficients, are varied.

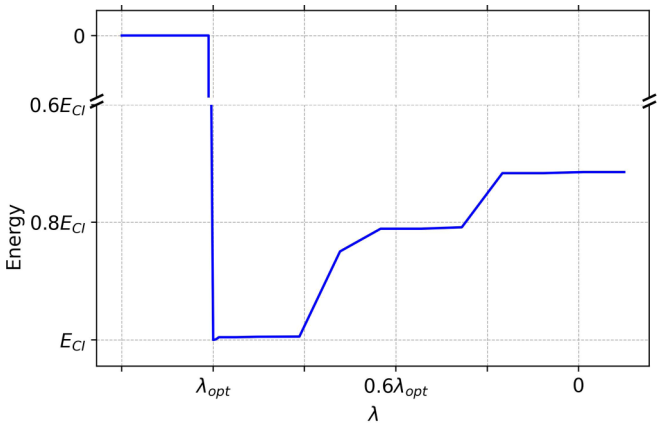

FIG. 2. Variation of energy E with λ, while minimizing the energy functional ϵ.

Next, we briefly explain the approach we have taken for our choice of λ in each Repeat. Figure 2 shows the variation of the optimized energy with λ. Note that each data point in the figure, that is, the optimized energy for a given value of λ, is obtained by minimizing Eq. (3) with respect to the CI coefficients on the classical optimizer. The QAE algorithm should ideally have the value $\lambda = \lambda_{\text{opt}}$, for which the optimized energy is minimum (and is equal to the relCI energy). In previous implementations of QAE, the optimal normalization penalty λ_{opt} over an appropriate range of λ is found by either scanning [17] or through bisection [18]. In our work, as discussed earlier, we chose the CSF energy corresponding to the dominant configuration as the initial value for λ. Subsequently, for each Repeat, we set the value of λ to the energy obtained from the previous Repeat. From the CI method, we know that λ_{opt} should be equal to E_{relCI}. This choice of the initial guess of λ is based on physical grounds and requires fewer Repeats than the previously proposed scanning [17] and bisection [18] methods.

The strategy of subspace optimization involves solving a sub-QUBO of qubits corresponding to the most dominant coefficients in the priority list. The first Repeat selected the first Γ dominant coefficients, allowing us to perform annealing for the subspace with highest variation in the energy. The next Γ lower-order configurations are added successively in this way through the following Repeats. When all the coefficients are included in this way after a few Repeats, we start over again, thereby leading to further tuning of the coefficients. Note that, during this method, λ, σ, and μ_α also vary appropriately.

We now discuss the embedding procedure, which embeds a densely connected QUBO to the D-wave QPU's topology by mapping some logical qubits to many hardware qubits

TABLE I. Individual energies of chosen systems for $^2P_{1/2}$ and $^2P_{3/2}$ states obtained using relCI, Simulation (S) and Hardware (H), and their corresponding standard deviation. In the table, "relCI" refers to the results obtained from relativistic configuration interaction (in Ha), "Simulation" gives our mean relativistic QAE results from a traditional computer (over five repetitions), but with hardware aspects such as connectivity taken into account, while the column "Hardware" gives the mean QAE results on the D-Wave Advantage machine (over five repetitions). SD refers to the standard deviation.

		Ca^{15+}	Fe^{21+}	Kr^{31+}	Mo^{37+}
$^2P_{1/2}$	relCI	−507.679395	−878.442367	−1730.364613	−2387.586842
	Simulation	−507.679333	−878.442308	−1730.364491	−2387.586714
	SD (S)	4.93E-05	3.17E-05	3.18E-05	2.93E-05
	Hardware	−507.679348	−878.442291	−1730.364520	−2387.586660
	SD (H)	1.61E-05	4.86E-05	4.61E-05	8.04E-05
$^2P_{3/2}$	relCI	−507.515951	−877.910029	−1728.136140	−2383.218738
	Simulation	−507.515819	−877.909781	−1728.135656	−2383.218002
	SD (S)	5.76E-05	9.63E-05	1.67E-04	1.74E-04
	Hardware	−507.515675	−877.909719	−1728.135639	−2383.218125
	SD (H)	9.24E-05	1.01E-04	1.41E-04	1.86E-04

and strongly coupling these hardware qubits together. This method is called chaining, and therefore, increases the number of qubits required. In this work, we focus on optimizing the strength of the coupling, called the chain strengths such that the chained qubits remain strongly coupled during quantum annealing, but also at the same time do not dominate the QUBO model's energy. After testing different strategies in simulations, we found that using the RMS of the subproblem's quadratic biases along with a multiplicative factor set between 0.75 and 1 gave the best results.

The annealing step consists of providing the subproblem adapted to the Pegasus topology of the D-Wave Advantage device to the quantum annealer and obtaining a fixed number of samples each time (which we set to 1000). We note that the samples here refer to the coefficients in the qubit space.

The composition and postprocessing steps involve merging the obtained samples with the main sample, back-converting them to the expansion coefficients, scaling them individually, and finally comparing with the known best solution from previous Repeats. The main sample refers to the solution of the complete QUBO problem (initialized to zeros). Scaling here refers to scaling $\{a_\alpha\}$ such that their absolute maximum becomes -1. This allows us to increase the smaller coefficients so that they can be captured with fewer qubits per coefficient (K), and deters the iterative optimization to navigate toward trivial wave-function solutions. The scaling step does not degrade the result because the normalization condition is not strictly imposed but rather with the addition of a penalty. After each Repeat, the subset of coefficients, σ, μ_α, and λ are changed in a systematic manner, and after several Repeats, we select the lowest energy among all Repeats.

We now comment on the information exchanged between the classical and quantum devices in the QAE workflow. The feedback efficiency depends on the size of the data being transmitted between the classical and quantum computers. At every Repeat, the coefficients A, B, and C are sent to the quantum annealer, where the dimension of A is $(K \times \mathcal{B})^2$, and that of B is $K \times \mathcal{B}$, while C has one real number. The values of q_n^α are obtained back from the annealer, which will have $K \times \mathcal{B} \times S$ binary values. Here, S is the number of samplings done per Repeat.

We carried out our implementation using the existing modules of D-Wave's OCEAN [43] and HYBRID [44] software development kits. Throughout this work $K = 10$.

III. RESULTS

In Tables I and II, we present our results for the energies of the $^2P_{1/2}$ and the $^2P_{3/2}$ states of Ca^{15+}, Fe^{21+}, Kr^{31+}, and Mo^{37+}, using QAE as well as the FSS values that we obtain from them, respectively. We also compare them with data from our numerical relCI computations and experiments. Our QAE computations were carried out both on traditional (simulation [45]) and quantum annealing (D-Wave Advantage) hardware. We note that our simulation results account for qubit connectivity. Figure 3 is a visual representation of the errors in the individual energies with respect to relCI energies. Our results from that figure show that our QAE approach can predict not only the FSS values, but also the individual energies to within 2.6×10^{-5} percentage. Our hardware results agree with the simulation and relCI computations to within 0.1 mHa. Finally, it is important to stress that our FSS values agree with the experimental results to around 99% on the average. In comparison, on a typical current-day gate-based quantum hardware, the errors in even the ground-state energies are much larger for a very simple four-qubit

TABLE II. FSS values for boron-like ions. "relCI" refers to numerical relativistic CI calculations (in Ha), "Simulation" and "Hardware" gives our mean (over five repetitions) of relativistic QAE performed on a traditional computer (with qubit connectivity taken into account) and D-Wave Advantage machine respectively. $\Delta_X\% = \frac{E_{\text{relCI}} - E_X}{\text{relCI}} \times 100$. "Expt." stands for the experimental value (in Ha).

System	relCI	Simulation ($\Delta_S \times 10^{-2}\%$)	Hardware ($\Delta_H \times 10^{-2}\%$)	Expt.
Ca^{15+}	0.1634	0.1635(−0.04)	0.1636(−0.14)	0.1668
Fe^{21+}	0.5323	0.5325(−0.04)	0.5325(−0.04)	0.5388
Kr^{31+}	2.2284	2.2288(−0.02)	2.2288(−0.02)	2.2442
Mo^{37+}	4.3681	4.3687(−0.01)	4.3685(−0.01)	4.3939

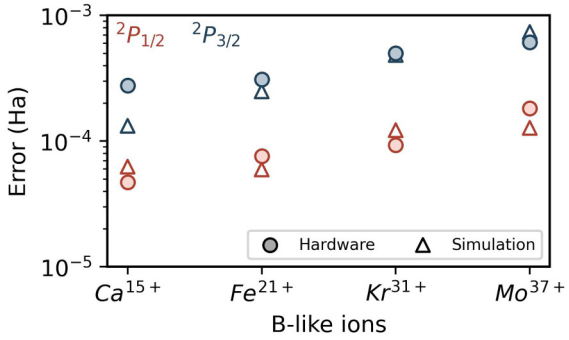

FIG. 3. Error with respect to relCI in QAE with Simulation that takes into account connectivity and with the D-Wave QPU for $^2P_{1/2}$ and $^2P_{3/2}$ states for all the considered ions.

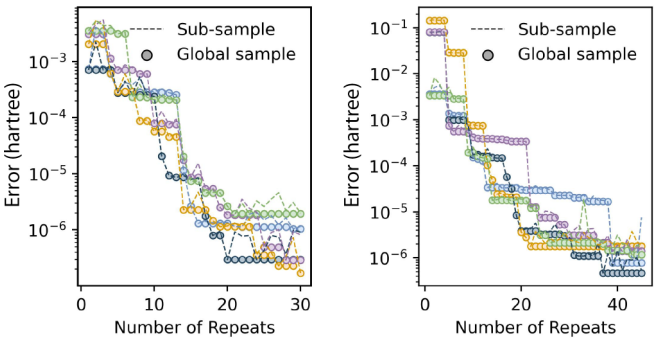

FIG. 4. Error in energy with respect to relCI versus number of Repeats in our workflow for (a) $^2P_{1/2}$ and (b) $^2P_{3/2}$ states of B-like Kr using the D-Wave Advantage QPU with steepest descent. The dashed lines present the error at every repeat, while circles present the error of the global sample. Different colors denote different repetition of the experiment.

Variational Quantum Eigensolver computation involving the H_2 molecule in a minimal basis.

The accuracy of our results is due to the inclusion of the important physics and computational attributes that are appropriate for the evaluation of the FSS of atomic systems. This includes the addition of Breit interaction in the Hamiltonian, choosing the same set of optimized orbitals for the $J = 1/2$ and $J = 3/2$ states of boron-like ions, as well as workflow improvements such as our floating qubit encoding scheme, updating lambda iteratively with the information of energy from previous iterations, priority ordering of the expansion coefficients on the basis of perturbation theory, and finally small adjustments such as tuning the coefficient of the RMS of biases. The MCDF orbital optimization can be improved even further, thereby improving the atomic states, but nevertheless, it is useful for demonstrating the QAE approach with a larger configuration space.

As a possible future extension, we could consider appending an optimization routine (for example, a discrete analog of steepest descent) as a local search algorithm at the end of each repeat. We considered a representative system, B-like Kr, and carried out the aforementioned procedure, termed "hybrid sampling." Our results for the percentage fraction difference with respect to relCI are presented in Table III. Figure 4 presents the error (difference in the energy from relCI and energy from QAE algorithm) with the number of Repeats for a representative system (boron-like Krypton), using the hybrid approach. Although the hybrid approach attains a given precision in a lower number of Repeats, it involves additional computational cost. Our future directions could involve employing more sophisticated many-body methods in combination with hybrid workflows with other optimizers.

TABLE III. Percentage fractional difference of energies of $^2P_{1/2}$ and $^2P_{3/2}$ states for B-like Kr from simulation (S), hardware (H), and hybrid sampler (HS) with respect to relCI. Hybrid sampler here refers to the computation performed on D-Wave Advantage with steepest descent optimizer.

State	relCI (Ha)	$\Delta_S \times 10^{-5}\%$	$\Delta_H \times 10^{-5}\%$	$\Delta_{HS} \times 10^{-5}\%$
$^2P_{1/2}$	−1730.3646	0.70	0.53	4.30×10^{-3}
$^2P_{3/2}$	−1728.1361	2.80	2.90	5.42×10^{-3}

We now discuss the stopping criterion adopted in this work. We begin by seeking a precision of at least 10^{-3}, that is, $E_{\text{relCI}} - E_{\text{QAE}}$ to be at least 10^{-3} with a high probability. We select r, the number of Repeats, by scanning datasets for a given state, such as $^2P_{1/2}$, and repeating runs five times per atomic system. We pick the maximum r where an error of 10^{-3} is reached in each of the 20 resulting curves and set $2r$ as the stopping criterion for hardware. The additional multiplicative factor of 2 is introduced, keeping in mind the limitations of the current state-of-the-art hardware. For $^2P_{3/2}$ states, we use $1.5r$ as the stopping criterion due to the larger matrix size and higher computation cost. Lastly, we chose the subQUBO sizes as an integral factor of the total QUBO size for convenience. Based on the above considerations, we chose $r = 30$ for $^2P_{1/2}$ states and $r = 45$ for $^2P_{3/2}$ states, with subQUBO sizes given in Table IV. The relevant data on $E_{\text{relCI}} - E_{\text{QAE}}$ versus the number of Repeats are presented in Figs. 5 and 6.

We now proceed to a brief discussion on possible sources of errors in our computations, which could arise from three factors: hardware errors, errors due to chaining, and approximations made in the construction of the QUBO form. For B-like Kr, we obtained an error of 9.3×10^{-5} Ha for the computation of $J = 1/2$ ground state using D-Wave quantum annealers. We also performed the same calculations using simulated annealing with D-Wave Advantage 5000-qubit architecture and obtained an error of 6.4×10^{-5} Ha. That is, we observed that the difference in the results obtained from simulated annealing and quantum annealing carried out on

TABLE IV. Workflow parameters for our QAE computations. We note that SubQUBO refers to the size of Γ after encoding.

State	QUBO size	SubQUBO size	Total Repeats
$^2P_{1/2}$	90	30	30
$^2P_{3/2}$	160	40	45

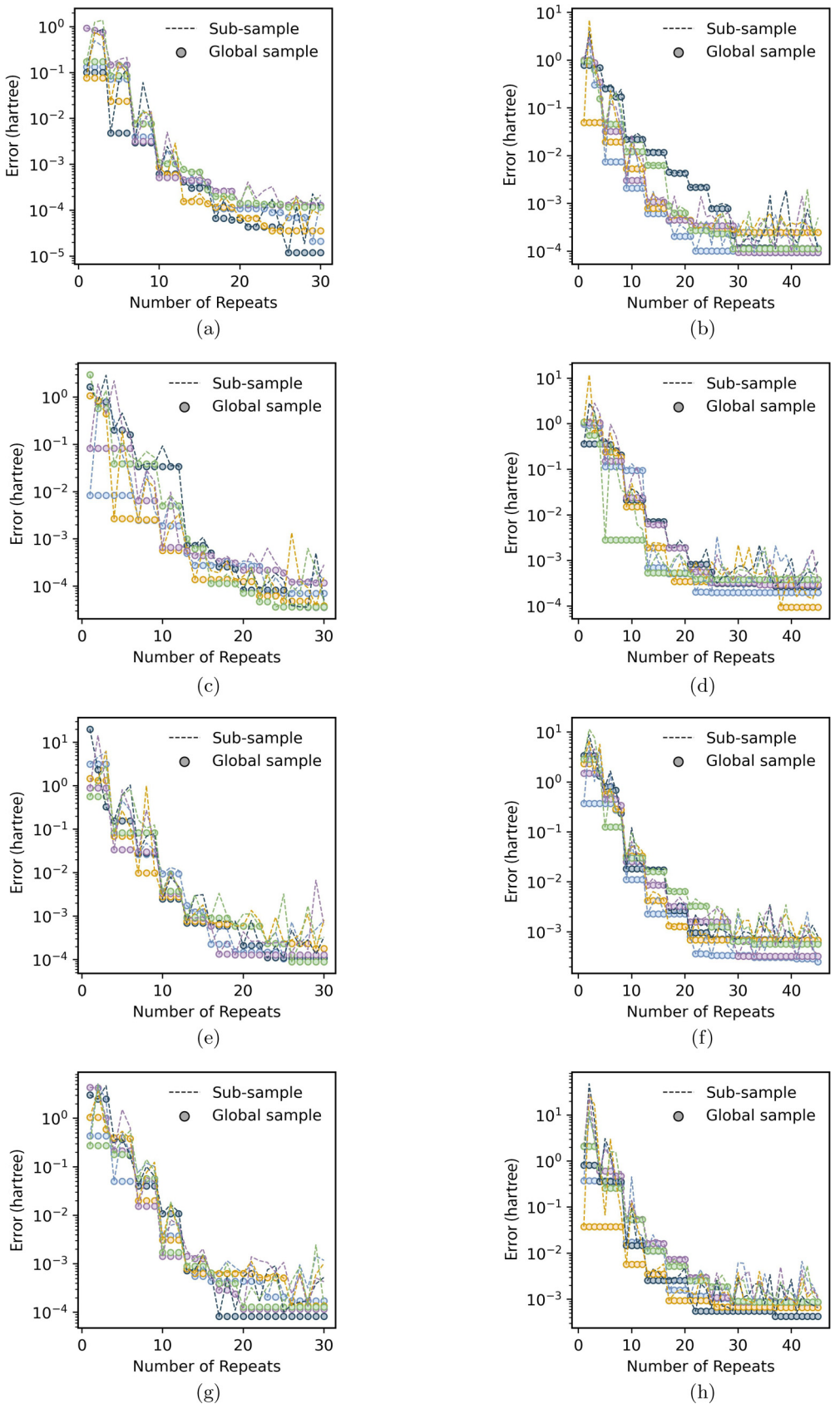

FIG. 5. Error in energy with respect to relCI versus number of Repeats in our workflow for (a), (c), (d), and (f) $^2P_{1/2}$ and (b), (d), (f), and (h) $^2P_{3/2}$ states of all the considered boron-like atoms using the simulation, taking hardware architecture into consideration. The dashed lines present the error at every repeat, while circles denote the error in the global sample. Different colors denote different repetitions of the experiment. Panels (a,b), (c,d), (e,f), and (g,h) correspond to boron-like Ca, Fe, Kr, and Mo, respectively.

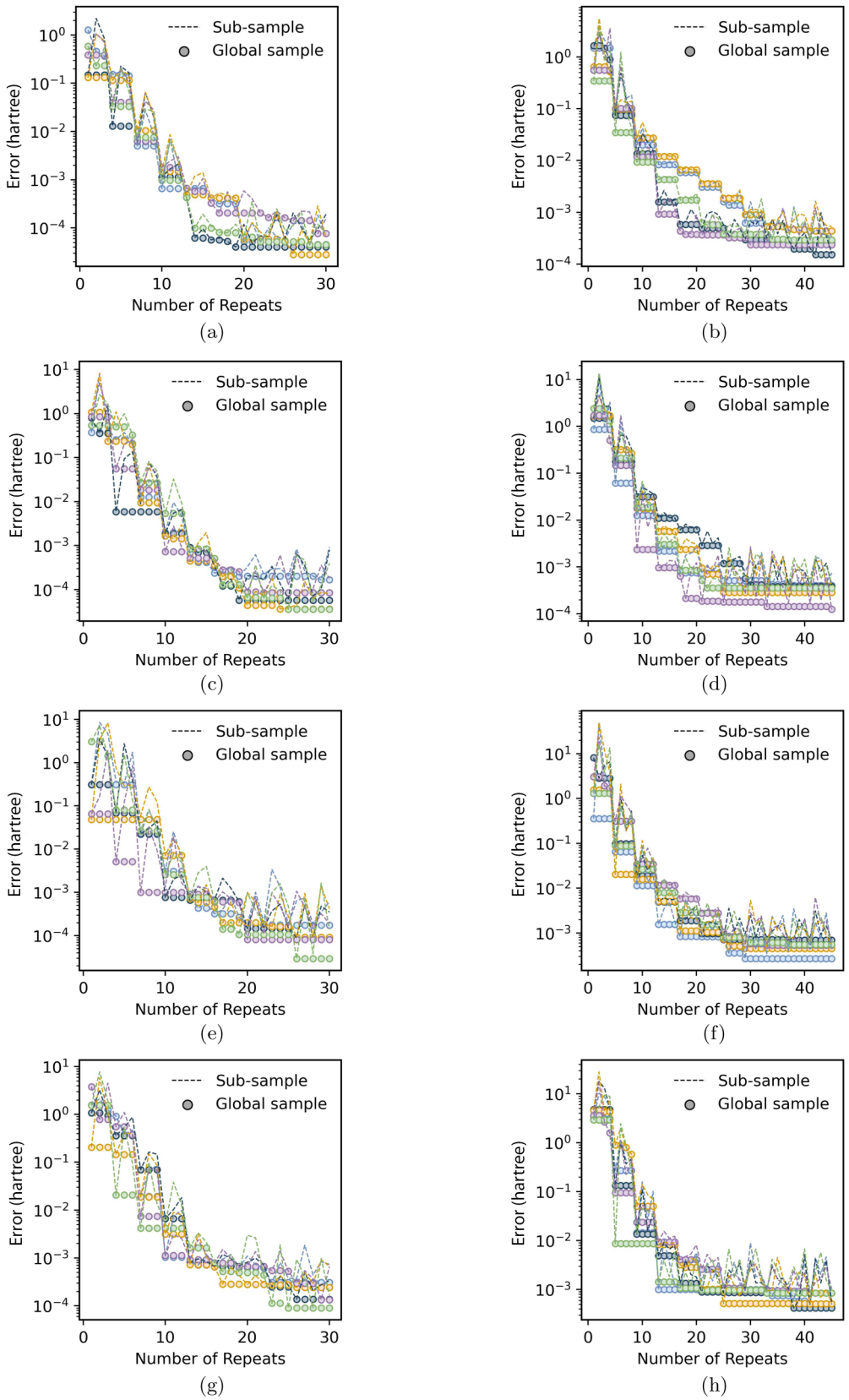

FIG. 6. Error in energy with respect to relCI versus number of Repeats in our workflow for (a), (c), (d), and (f) $^2P_{1/2}$ and (b), (d), (f), and (h) $^2P_{3/2}$ states of all the considered boron-like atoms using the D-Wave hardware. The dashed lines present the error at every repeat, while circles denote the error in the global sample. Different colors denote different repetitions of the experiment. Panels (a,b), (c,d), (e,f), and (g,h) correspond to boron-like Ca, Fe, Kr, and Mo, respectively.

hardware was negligible. Expecting that simulated annealing and ideal quantum hardware results match, we infer that the error from hardware toward determining FSS may be negligible. The explanation could be that 1000 anneals makes our approach fairly robust to noise. Finally, we performed simulated annealing assuming all-to-all connectivity and obtained an error of 1.4×10^{-7} Ha. We expect that this error comes from approximations made in QUBO generation (our choice of $K = 10$ in our floating point encoding scheme). The deviation between simulations with D-Wave Advantage hardware connectivity and all-to-all connectivity is the most significant. Hence the effect of chaining on D-Wave devices is the limiting factor for accuracy in our findings. We end the discussion with a comment on the possibility of encountering a barren plateau. The variational parameters are the CI coefficients in the QAE algorithm, as opposed to parameters that occur in the functional form of an ansatz in the case of VQE. Since the energy changes as the coefficients are varied, we do not expect to encounter a barren plateau in our QAE work, which is based on complete active space CI.

IV. CONCLUSION AND FUTURE OUTLOOK

In summary, we developed the relativistic version of the QAE algorithm, which computes the minimum eigenvalues corresponding to specific atomic symmetries, and conducted a pilot study to calculate fine-structure splittings in the boron-like atomic ions (Ca^{15+}, Fe^{21+}, Kr^{31+}, and Mo^{37+}). The method of eigenvalue estimation through quantum annealing may be of practical relevance for a diverse range of problems. Salient features of our work involve improving the QAE workflow and includes an improved optimization strategy for the Lagrange multiplier occurring in the energy functional, priority listing of the CI coefficients, and floating qubit encoding method. With these improvements in place, we carried out relativistic calculations on both traditional computers as well as on quantum hardware. In the former, the simulations were carried out by accounting for the absence of all-to-all connectivity on the D-Wave devices. We find that our hardware results for fine-structure splitting yield an average deviation of 1.1 percent with respect to experiments and 2.71×10^{-2} percent with respect to the relativistic CI calculations that we use to benchmark our results. We stress that our implementation allows us to accurately predict the individual energies of the states, thus enabling us to predict the fine-structure splitting, which is an energy difference, accurately. To that end, we add that the individual energies themselves were evaluated to be within $\sim 5 \times 10^{-5}$ percent of relativistic CI energies.

Our work marks the first demonstration of relativistic many-body calculations carried out on quantum annealers. Our accurate results can be considered a stepping stone to future relativistic atomic and molecular calculations for novel applications, including probing new physics beyond the standard model of elementary particles. Such applications require carrying out high accuracy computations on large atomic systems, including superheavy elements. We envision the realization of such calculations for large atomic systems in view of the ongoing advances on the quantum annealing hardware front. We recall that a typical QAE calculation can be broken down into three sequential steps: the generation of the Hamiltonian matrix, encoding the functional, and annealing. Solving the state-averaged multiconfiguration Dirac-Fock (MCDF) coupled differential equations enables relatively less expensive overheads in encoding, but such differential equation-based approaches are known to be plagued by severe convergence issues as the system size increases [46]. However, there have been promising developments recently in quantum annealing algorithms for differential equations, for example, the QADE algorithm [47], where the authors indicated that one can expect to solve coupled differential equations efficiently for large system sizes with more qubits and better connectivity. If such quantum algorithms are realized in more powerful quantum annealers in the future, they would open new avenues to treat larger atomic systems via the differential equation-based MCDF methods, essentially opening up opportunities even for quantum utility, where quantum computers can solve certain problems for system sizes where classical devices fail. We also note that new architectures such as LHZ [48] and generalizations such as ParityQC (see Refs. [49,50]; and whose first implementation was recently carried out by AIST-NEC, Japan) and the Zephyr (from D-Wave) [51] may offer alternative relatively cheaper approaches to embedding (which will have significant implications for both the third step of QAE and also for improving the efficiency of differential equations-based approaches). We expect that a combination of an efficient pre-processing quantum algorithm for solving MCDF differential equations, novel architectures, efforts to increase coherence times [52,53], and error mitigation schemes (for example, see Refs. [54,55]) can pave the way for potential quantum utility.

ACKNOWLEDGMENTS

The classical computations were done on Rudra (Sankhya-Sutra Labs) supercomputers. The AWS Braket platform was used for cloud access to D-Wave Advantage 6.1 Hardware through the credits provided by the Ministry of Electronics and Information Technology (MeitY) Quantum Computing Applications Lab (QCAL) Cohort 1 project (N-21/17/2020-NeGD, 2022-2024). K.S. acknowledges support from "Quantum Software" project (Grant No. JPMJPR1914) from Japan Science and Technology Agency (JST), Japan, Center of Innovations for Sustainable Quantum AI (Grant No. JPMJPF2221) from JST, Japan, and Quantum Leap Flagship Program (Grant No. JPMXS0120319794) from Ministry of Education, Culture, Sports, Science and Technology, Japan.

[1] P. Hauke, H. G. Katzgraber, W. Lechner, H. Nishimori, and W. D. Oliver, Perspectives of quantum annealing: methods and implementations, Rep. Prog. Phys. **83**, 054401 (2020).

[2] T. Kadowaki and H. Nishimori, Quantum annealing in the transverse Ising model, Phys. Rev. E **58**, 5355 (1998).

[3] S. Yarkoni, E. Raponi, T. Bäck, and S. Schmitt, Quantum annealing for industry applications: introduction and review, Rep. Prog. Phys. **85**, 104001 (2022).

[4] B. K. Chakrabarti, H. Leschke, P. Ray, T. Shirai, and S. Tanaka, Quantum annealing and computation: Challenges and perspectives, Philos. Trans. R. Soc. A **381**, 20210419 (2023).

[5] E. J. Crosson and D. A. Lidar, Prospects for quantum enhancement with diabatic quantum annealing, Nat. Rev. Phys. **3**, 466 (2021).

[6] V. Canivell, P. Forn-Díaz, A. Garcia-Saez, and R. Sagastizabal, Startup Qilimanjaro—towards a European full-stack coherent quantum annealer platform, EPJ Quantum Technology **8**, 6 (2021).

[7] S. Weber, J. Cummings, J. Miloshi, K. Thompson, J. Rokosz, D. Holtman, D. Conway, A. Kerman, and W. Oliver, High-density I/O for next-generation quantum annealing: Part 1-Cryogenic wiring, in *APS March Meeting Abstracts*, APS Meeting Abstracts, Vol. 2021 (APS, College Park, MD, 2021), p. M30.008.

[8] A. Mott, J. Job, J. R. Vlimant, D. Lidar, and M. Spiropulu, Solving a Higgs optimization problem with quantum annealing for machine learning, Nature (London) **550**, 375 (2017).

[9] R. Y. Li, R. Di Felice, R. Rohs, and D. A. Lidar, Quantum annealing versus classical machine learning applied to a simplified computational biology problem, npj Quantum Inf. **4**, 14 (2018).

[10] H. Irie, H. Liang, T. Doi, S. Gongyo, and T. Hatsuda, Hybrid quantum annealing via molecular dynamics, Sci. Rep. **11**, 8426 (2021).

[11] A. D. King, S. Suzuki, J. Raymond, A. Zucca, T. Lanting, F. Altomare, A. J. Berkley, S. Ejtemaee, E. Hoskinson, S. Huang, E. Ladizinsky, A. J. R. MacDonald, G. Marsden, T. Oh, G. Poulin-Lamarre, M. Reis, C. Rich, Y. Sato, J. D. Whittaker, J. Yao *et al.*, Coherent quantum annealing in a programmable 2,000 qubit Ising chain, Nat. Phys. **18**, 1324 (2022).

[12] K. Kitai, J. Guo, S. Ju, S. Tanaka, K. Tsuda, J. Shiomi, and R. Tamura, Designing metamaterials with quantum annealing and factorization machines, Phys. Rev. Res. **2**, 013319 (2020).

[13] D. Inoue, A. Okada, T. Matsumori, K. Aihara, and H. Yoshida, Traffic signal optimization on a square lattice with quantum annealing, Sci. Rep. **11**, 3303 (2021).

[14] S. Matsuura, T. Yamazaki, V. Senicourt, L. Huntington, and A. Zaribafiyan, VanQver: the variational and adiabatically navigated quantum eigensolver, New J. Phys. **22**, 053023 (2020).

[15] R. Xia, T. Bian, and S. Kais, Electronic structure calculations and the Ising Hamiltonian, J. Phys. Chem. B **122**, 3384 (2018).

[16] M. Streif, F. Neukart, and M. Leib, Solving quantum chemistry problems with a D-wave quantum annealer, in *Quantum Technology and Optimization Problems*, edited by S. Feld and C. Linnhoff-Popien (Springer International Publishing, Cham, Germany, 2019), pp. 111–122.

[17] A. Teplukhin, B. K. Kendrick, and D. Babikov, Calculation of molecular vibrational spectra on a quantum annealer, J. Chem. Theory Comput. **15**, 4555 (2019).

[18] A. Teplukhin, B. K. Kendrick, S. Tretiak, and P. A. Dub, Electronic structure with direct diagonalization on a D-wave quantum annealer, Sci. Rep. **10**, 20753 (2020).

[19] A. Teplukhin, B. K. Kendrick, S. M. Mniszewski, Y. Zhang, A. Kumar, C. F. Negre, P. M. Anisimov, S. Tretiak, and P. A. Dub, Computing molecular excited states on a D-Wave quantum annealer, Sci. Rep. **11**, 18796 (2021).

[20] A. L. Price, N. J. Patterson, R. M. Plenge, M. E. Weinblatt, N. A. Shadick, and D. Reich, Principal components analysis corrects for stratification in genome-wide association studies, Nat. Genet. **38**, 904 (2006).

[21] N. Bender, A. Yamilov, H. Yılmaz, and H. Cao, Fluctuations and correlations of transmission eigenchannels in diffusive media, Phys. Rev. Lett. **125**, 165901 (2020).

[22] O. Diekmann, J. A. P. Heesterbeek, and J. A. J. Metz, On the definition and the computation of the basic reproduction ratio R_0 in models for infectious diseases in heterogeneous populations, J. Math. Biol. **28**, 365 (1990).

[23] P. L. Roe, Characteristic-based schemes for the Euler equations, Annu. Rev. Fluid Mech. **18**, 337 (1986).

[24] M. Turk and A. Pentland, Eigenfaces for recognition, J. Cognit. Neurosci. **3**, 71 (1991).

[25] P. Pyykkö, Relativistic effects in chemistry: More common than you thought, Annu. Rev. Phys. Chem. **63**, 45 (2012).

[26] R. Ahuja, A. Blomqvist, P. Larsson, P. Pyykkö, and P. Zaleski-Ejgierd, Relativity and the lead-acid battery, Phys. Rev. Lett. **106**, 018301 (2011).

[27] V. A. Dzuba, V. V. Flambaum, M. T. Murphy, and D. A. Berke, Relativistic frequency shifts in Cr, Ti, Fe, Ni, Ca, Na, and V to search for variations in the fine-structure constant, Phys. Rev. A **105**, 062809 (2022).

[28] V. V. Flambaum and H. B. Tran Tan, Oscillating nuclear electric dipole moment induced by axion dark matter produces atomic and molecular electric dipole moments and nuclear spin rotation, Phys. Rev. D **100**, 111301(R) (2019).

[29] B. K. Sahoo, T. Aoki, B. P. Das, and Y. Sakemi, Enhanced spin-dependent parity-nonconservation effect in the $7s^2 s_{1/2} \rightarrow 6d^2 d_{5/2}$ transition in Fr: A possibility for unambiguous detection of the nuclear anapole moment, Phys. Rev. A **93**, 032520 (2016).

[30] B. K. Sahoo and B. P. Das, Relativistic normal coupled-cluster theory for accurate determination of electric dipole moments of atoms: First application to the ^{199}Hg atom, Phys. Rev. Lett. **120**, 203001 (2018).

[31] B. K. Sahoo, High-precision determination of Lorentz-symmetry-violating parameters in Ca^+, Phys. Rev. A **99**, 050501(R) (2019).

[32] Y. M. Yu and B. K. Sahoo, Selected highly charged ions as prospective candidates for optical clocks with quality factors larger than 10^{15}, Phys. Rev. A **97**, 041403(R) (2018).

[33] B. P. Das, J. Hata, and I. P. Grant, Ground-state fine structure in the boron isoelectronic sequence, J. Phys. B **17**, L1 (1984).

[34] B. P. Das, K. V. P. Latha, B. K. Sahoo, C. Sur, R. K. Chaudhuri, and D. Mukherjee, Relativistic and correlation effects in atoms, J. Theor. Comput. Chem. **04**, 1 (2005).

[35] M. Booth, S. P. Reinhardt, and A. Roy, Partitioning Optimization Problems for Hybrid Classical/Quantum Execution, D-Wave Technical Report Series (2017), https://docs.ocean.dwavesys.com/projects/qbsolv/en/latest/_downloads/bd15a2d8f32e587e9e5997ce9d5512cc/qbsolv_techReport.pdf.

[36] B. Edlén, Comparison of theoretical and experimental level values of the $n = 2$ configurations in the boron isoelectronic sequence, Phys. Scr. **28**, 483 (1983).

[37] E. Hinnov and S. Suckewer, Magnetic dipole transitions in highly ionized titanium, chromium, iron and nickel, Phys. Lett. A **79**, 298 (1980).

[38] B. Denne, E. Hinnov, J. Ramette, and B. Saoutic, Spectrum lines of kr xxviii–kr xxxiv observed in the JET tokamak, Phys. Rev. A **40**, 1488 (1989).

[39] R. Myrnäs, C. Jupén, G. Miecznik, I. Martinson, and B. Denne-Hinnov, Transitions in boron-like Ni XXIV, Ge XXVIII, Kr XXXII and Mo XXXVIII and fluorinelike Zr XXXII and Mo XXXIV, observed in the JET tokamak, Phys. Scr. **49**, 429 (1994).

[40] *Relativistic Quantum Theory of Atoms and Molecules*, edited by I. P. Grant (Springer, New York, 2007), p. 325.

[41] *Relativistic Quantum Theory of Atoms and Molecules*, edited by I. P. Grant (Springer, New York, 2007), p. 339.

[42] F. A. Parpia and I. P. Grant (unpublished).

[43] GitHub, D-Wave Systems, "Ocean" repository, https://github.com/dwavesystems/dwave-ocean-sdk (2022).

[44] GitHub, D-Wave Systems, "Hybrid" repository, https://github.com/dwavesystems/dwave-hybrid (2022).

[45] S. Kirkpatrick, C. D. Gelatt, and M. P. Vecchi, Optimization by simulated annealing, Science **220**, 671 (1983).

[46] P. Jönsson *et al.*, An introduction to relativistic theory as implemented in GRASP, Atoms **11**, 7 (2022).

[47] J. C. Criado and M. Spannowsky, Qade: solving differential equations on quantum annealers, Quantum Sci. Technol. **8**, 015021 (2023).

[48] W. Lechner, P. Hauke, and P. Zoller, A quantum annealing architecture with all-to-all connectivity from local interactions, Sci. Adv. **1**, e1500838 (2015).

[49] M. Fellner, A. Messinger, K. Ender, and W. Lechner, Universal parity quantum computing, Phys. Rev. Lett. **129**, 180503 (2022).

[50] R. ter Hoeven, A. Messinger, and W. Lechner, Flexible constraint compilation in the parity architecture, Phys. Rev. A **108**, 042606 (2023).

[51] K. Boothby, A. D. King, and J. Raymond, Zephyr Topology of D-Wave Quantum Processors, D-Wave Technical Report Series (2021), https://www.dwavesys.com/media/2uznec4s/14-1056a-a_zephyr_topology_of_d-wave_quantum_processors.pdf.

[52] S. Novikov, R. Hinkey, S. Disseler, J. I. Basham, T. Albash, A. Risinger, D. F. D. A. Lidar, and K. M. Zick, Exploring more-coherent quantum annealing, in *Proceedings of the 2018 IEEE International Conference on Rebooting Computing (ICRC), McLean, VA* (IEEE, Piscataway, NJ, 2018), pp. 1–7.

[53] J. A. Grover, J. I. Basham, A. Marakov, S. M. Disseler, R. T. Hinkey, M. Khalil, Z. A. Stegen, T. Chamberlin, W. DeGottardi, D. J. Clarke, J. R. Medford, J. D. Strand, M. J. A. Stoutimore, S. Novikov, D. G. Ferguson, D. Lidar, K. M. Zick, and A. J. Przybysz, Fast, lifetime-preserving readout for high-coherence quantum annealers, PRX Quantum **1**, 020314 (2020).

[54] Y. Shingu, T. Nikuni, S. Kawabata, and Y. Matsuzaki, Quantum annealing with error mitigation, arXiv:2210.08862.

[55] M. H. Amin, A. D. King, J. Raymond, R. Harris, W. Bernoudy, A. J. Berkley, K. Boothby, A. Smirnov, F. Altomare, M. Babcock, C. Baron, J. Connor, M. Dehn, C. Enderud, E. Hoskinson, S. Huang, M. W. Johnson, E. Ladizinsky, T. Lanting, A. J. R. MacDonald, G. Marsden, R. Molavi, T. Oh, G. Poulin-Lamarre, H. Ramp *et al.*, Quantum error mitigation in quantum annealing, arXiv:2311.01306.